

Slim disk modeling reveals an accreting intermediate-mass black hole in the luminous fast blue optical transient AT2018cow

Zheng Cao^{1,2,*}, Peter G. Jonker^{2,1}, Sixiang Wen³, and Ann I. Zabludoff⁴

¹ SRON, Netherlands Institute for Space Research, Niels Bohrweg 4, 2333 CA, Leiden, The Netherlands

² Department of Astrophysics/IMAPP, Radboud University, P.O. Box 9010, 6500 GL, Nijmegen, The Netherlands

³ National Astronomical Observatories, Chinese Academy of Sciences, 20A Datun Road, Beijing 100101, China

⁴ University of Arizona, 933 N. Cherry Ave., Tucson, AZ 85721

Received XXX; accepted XXX

ABSTRACT

The origin of the most luminous subclass of the fast blue optical transients (LFBOTs) is still unknown. We present an X-ray spectral analysis of AT2018cow—the LFBOT archetype—using *NuSTAR*, *Swift*, and *XMM-Newton* data. The source spectrum can be explained by the presence of a slim accretion disk, and we find that the mass accretion rate decreases to sub-Eddington levels $\gtrsim 200$ days after the source's discovery. Applying our slim disk model to data obtained at multiple observational epochs, we constrain the mass of the central compact object in AT2018cow to be $\log(M_{\bullet}/M_{\odot}) = 2.4_{-0.1}^{+0.6}$ at the 68% confidence level. Our mass measurement is independent from, but consistent with, the results from previously employed methods. The mass constraint is consistent with both the tidal disruption and the black hole–star merger scenarios, if the latter model can be extrapolated to the measured black hole mass. Our work provides evidence for an accreting intermediate-mass black hole (10^2 – $10^6 M_{\odot}$) as the central engine in AT2018cow, and, by extension, in LFBOT sources similar to AT2018cow.

Key words. X-ray astronomy – accretion physics – fast blue optical transient

1. Introduction

Fast Blue X-ray Transients (FBOTs; e.g., Drout et al. 2014; Arcavi et al. 2016; Tanaka et al. 2016; Pursiainen et al. 2018; Tampo et al. 2020; Ho et al. 2022b, 2023) have attracted significant attention in recent years as their physical nature is not yet known. Those at the most luminous end ($\gtrsim 10^{44}$ erg s⁻¹) of the FBOT population are often referred to as Luminous FBOTs (LFBOTs). LFBOTs are characterized by a rapid optical rise and high peak luminosity (reaching the peak luminosity on a timescale of days; e.g., Drout et al. 2014; Pursiainen et al. 2018; Rest et al. 2018; Ho et al. 2023).

The archetype of LFBOTs is AT2018cow. AT2018cow was discovered on 2018-06-16 (Modified Julian Date, or MJD, 58285) by the ATLAS survey (Smartt et al. 2018). The host galaxy CGCG137-068 has a luminosity distance of ~ 60 Mpc (redshift $z = 0.01404$; Adelman-McCarthy et al. 2008). AT2018cow is the nearest LFBOT to Earth and has been observed across a broad energy range. Multi-wavelength observations show that the source emission extends from radio to γ -rays (e.g., Prentice et al. 2018; Rivera Sandoval et al. 2018; Kuin et al. 2019; Margutti et al. 2019; Perley et al. 2019; Ho et al. 2019; Nayana & Chandra 2021). In particular, X-ray emission was observed immediately after the source's discovery (Rivera Sandoval et al. 2018; Kuin et al. 2019). Analysis of the X-ray spectrum shows that the earliest deep X-ray observation of *NuSTAR*

could be well-described by reflection off an accretion disk (Margutti et al. 2019).

Different models have been proposed to explain the multi-wavelength behavior of AT2018cow, or AT2018cow-like LFBOTs (e.g., AT2020xnd/ZTF20acigmel, Perley et al. 2021; AT2020rmf, Yao et al. 2022). One class of scenarios involves an accreting compact object, either a neutron star (NS) or a black hole (BH), as the "central engine" for the highly-variable, non-thermal X-ray emission. Examples in this class of models include i) a tidal disruption event (TDE) involving an intermediate-mass black hole (IMBH, BH mass M_{\bullet} between 10^2 and $10^6 M_{\odot}$; Kuin et al. 2019; Perley et al. 2019); ii) a core-collapse event such as a supernova giving birth to the central compact object, which then accretes fall-back progenitor material (e.g., Prentice et al. 2018; Margutti et al. 2019; Perley et al. 2019; Mohan et al. 2020; Gottlieb et al. 2022); iii) a binary merger of a BH and its massive stellar companion (Metzger 2022).

Meanwhile, there is another class of models that relies exclusively on shock interactions in the circumstellar material (CSM; e.g., Rivera Sandoval et al. 2018; Fox & Smith 2019; Leung et al. 2021; Pellegrino et al. 2022). However, it is challenging for these models to explain the observed early-time X-ray/ γ -ray behavior without also invoking an accreting compact object (see, e.g., Margutti et al. 2019; Coppejans et al. 2020; Pasham et al. 2022; Yao et al. 2022; Metzger 2022; Migliori et al. 2023). Furthermore, late-time ($\gtrsim 200$ days since MJD 59295) observations of AT2018cow reveal a soft X-ray source spectrum (Migliori et al. 2023).

* z.cao@sron.nl

Moreover, the source enters a long-lasting "plateau" phase in the UV lightcurves (e.g., Inkenhaag et al. 2023), resembling a BH evolving from a high to a low mass accretion rate, which can last months to years (e.g., similar to what has been seen in many TDEs; van Velzen et al. 2019; Mummery & Balbus 2020; Wen et al. 2023; Cao et al. 2023; Mummery et al. 2024b).

The mass of the central compact object is of key importance to unveil the nature of AT2018cow-like LFBOTs. To that end, it is essential to compare different mass measurements to verify the different measurement methods. Several studies have reported (limits on) the compact object mass in AT2018cow. From an X-ray timing analysis, Pasham et al. (2022) find an upper limit on the central object mass of $\lesssim 850 M_{\odot}$, assuming the quasi-periodic oscillations in the arrival times of X-ray photons are due to particular orbital frequencies in an accretion disk (but see Zhang et al. 2022). Migliori et al. (2023) constrain the compact object mass to be $\approx 10 - 10^4 M_{\odot}$ based on energetic arguments, while Inkenhaag et al. (2023) find the mass to be $10^{3.2 \pm 0.8} M_{\odot}$ based on modeling of the late-time UV emission as coming from a TDE-like accretion disk. In this paper, we use X-ray spectral analysis to provide a mass measurement of the central compact object.

The paper is structured as follows: In Section 2, we describe the data and the data reduction method. In Section 3, we describe the slim disk model. In Section 4, we present the results from our analysis. In Section 5 we discuss the results and present our conclusions.

2. Methods and data reduction

In this study, we use Poisson statistics (Cash 1979; CSTAT in XSPEC). We quote all parameter errors at the 1σ (68%) confidence level, assuming $\Delta C\text{-stat} = 1.0$ and $\Delta C\text{-stat} = 2.3$ for single- and two-parameter error estimates, respectively. When needed, we use the Akaike information criteria (AIC; Akaike 1974) to investigate the significance of adding model components to the fit-function, which is calculated by $\Delta AIC = -\Delta C + 2\Delta k$ (C is the C-stat and k is the degree-of-freedom; Wen et al. 2018). The $\Delta AIC > 5$ and > 10 cases are considered a strong and very strong improvement, respectively, over the alternative model. For all the fits we perform in this paper, we include Galactic absorption using the model TBabs (Wilms et al. 2000). We fix the column density N_{H} to $5 \times 10^{20} \text{cm}^{-2}$ without considering any intrinsic absorption, consistent with the work by (Margutti et al. 2019; Migliori et al. 2023).

2.1. NuSTAR observations

AT2018cow was observed by NuSTAR on five occasions since 2018-06-23 (MJD 58292). Due to the decreasing of the X-ray flux above 3 keV, AT2018cow was not detected in the last NuSTAR observation (ObsID: 80502407002), and a count-rate upper limit of $1.1 \times 10^{-4} \text{ counts s}^{-1}$ has been inferred (Migliori et al. 2023). To perform spectral analysis, in this paper we only consider the first four NuSTAR observations, which were all taken within 37 days since the discovery of the source. A list of NuSTAR observations analyzed in this paper is presented in Table B.1. We perform the NuSTAR data reduction using NuSTARDAS version 1.9.7 with calibration files updated on 2023-10-17 (version 20231017). We use the pipeline tool NUPIPELINE to extract

the level-2 science data, and the tool NUPRODUCT to produce the source+background and background spectra from the level-2 data. For both FPMA and FPMB detectors onboard NuSTAR, the source+background spectra are extracted from a circular source region of $30''$ radius centered on the source. The background spectra are extracted from circular apertures of $> 50''$ radii close to the source on the same detector, free from other bright sources.

2.2. XMM-Newton observations

AT2018cow was observed by XMM-Newton on three occasions within 300 days after its discovery, and another three occasions in the year 2022. Because the source becomes too faint that the background flux dominates over the source+background flux, we discard the last three XMM-Newton observations (ObsID: 0843550401, 0843550501, 0843550601) in our subsequent analysis. We list the XMM-Newton observations used for the analysis presented in this paper in Table B.1. We reduce the XMM-Newton data using HEASOFT version 6.32.1 and SAS version 21.0.0 with calibration files renewed on October 5th, 2023 (CCF release: XMM-CCF-REL-402). During one of the observations (ObsID: 0822580501), one of the two MOS detectors onboard XMM-Newton was used for calibration and no science data was obtained. Meanwhile, the signal-to-noise ratio in the RGS detectors is too low to perform spectral analysis. Therefore, for consistency, we only use the data from the EPIC-pn detector.

We use the SAS task EPPROC to process the data. We employ the standard filtering criteria to exclude periods with an enhanced background count rate, requiring that the 10-12 keV detection rate of pattern 0 events is $< 0.4 \text{ counts s}^{-1}$. We use a circular source region of $25''$ radius centered on the source for the source+background spectral extraction. This extraction region is somewhat smaller than we would have used normally because it is designed to avoid contamination from nearby soft-X-ray sources and the detector edges. Using the SAS command EPATPLOT, we check for the presence of photon pile-up and find no evidence for effects caused by pile-up. The background spectra are extracted from circular apertures of $\gtrsim 40''$ radii close to the source on the same detector, free from other bright sources.

2.3. Swift observations

In this paper we also include the X-ray data from the Swift/XRT instrument. Swift monitored AT2018cow within the first 100 days after its discovery. We extract the X-ray lightcurve from Swift/XRT using the online data reduction pipeline¹ (Evans et al. 2009), applying the default reduction criteria. Meanwhile, using the same tool, we also extract the Swift/XRT source+background spectra as well as the background spectra (see Evans et al. 2009 for more details). Furthermore, for each of the NuSTAR epoch, we combine the extracted Swift/XRT spectra that are taken on the same date. In this way, we prepare the quasi-simultaneous Swift/XRT observations for joint spectral analysis with the NuSTAR observations. We present the information of these periods for the spectral count extraction in Table B.1.

Throughout this paper, we carry out spectral analysis using the XSPEC package (Arnaud 1996; version 12.13.1).

¹ https://www.swift.ac.uk/user_objects/

With the `ENERGIES` command in `XSPEC`, we create a logarithmic energy array of 1000 bins from 0.1 to 1000.0 keV for model calculations in all analyses for consistency. Using the `FTOOL FTGROUPPHA` for spectral analysis, we re-bin every background and source+background spectrum by the optimal-binning algorithm (Kaastra & Bleeker 2016), while requiring the spectra to have a minimum of 1 count per bin (with parameter `GROUPTYPE` in `FTGROUPPHA` set to `OPTMIN`). For every spectrum, we discard the data bins where the background flux is dominating over the source+background flux. The remaining energy bands in each spectrum for our spectral analysis are given in Table B.1.

For every remaining observation, we first fit the background spectrum using a phenomenological model. When fitting the source+background spectrum, we then add the best-fit background model to the fit-function describing the source+background spectrum, with the background model parameters all fixed to their best-fit values determined from the fit to the background-only spectrum. The best-fit background model varies from instrument to instrument, and from epoch to epoch. For the *XMM-Newton*EPIC-pn data, the best-fit phenomenological background model consists of between 2-3 power-law components and 2-3 Gaussian components; for *NuSTAR*, it consists of 2 power-law and 3 Gaussian components; for *Swift*, it consists of 2 power-law components. The full-width at half-maximum (FWHM) of every background Gaussian component is fixed to $\sigma_{\text{Gauss}} = 0.001$ keV, less than the spectral resolution of either *XMM-Newton*/EPIC-pn, *NuSTAR*, or *Swift*. Such phenomenological models account for both the background continuum and the fluorescence lines (e.g., Katayama et al. 2004; Pagani et al. 2007; Harrison et al. 2010). In this paper, when studying the source+background spectra, we refer only to the part of the fit function that describes the source as fit function.

We group all the data mentioned above into six epochs by time of the observations. A list of the epochs and the associated observations can be found in Table B.1. When performing spectral analysis, we always jointly fit the spectra within the same epoch using the same fit function for the source spectra. To account for the mission specific calibration differences, we use a constant component (`constant` in `XSPEC`) multiplying the source models. This constant serves as a re-normalization factor between different instruments. Specifically, we fix the constant to be 1 for *NuSTAR*/FPMA spectra, and let the constant for other instruments free-to-vary in the fits for each epoch.

3. Extending slim disk model `slimdz` to lower M_{\bullet}

The very luminous X-ray emissions from AT2018cow (peak luminosity $L_x \gtrsim 10^{44}$ erg s⁻¹) imply the source is in the super-Eddington regime at least for the early days when its X-rays are near the peak, if powered by accretion onto a BH of $10^1 - 10^3 M_{\odot}$. When the mass accretion rate is at near-/super-Eddington levels, the accretion disk can no longer be adequately described by a standard thin disk model (Shakura & Sunyaev 1973), as the inward advection of the liberated energy is no longer negligible (e.g., Abramowicz et al. 1988). Therefore, we choose to use a slim disk model, `slimdz` (Wen et al. 2022), to model the disk thermal emission from AT2018cow in our spectral analysis.

In its original form in Wen et al. 2022, the slim disk model `slimdz` does not allow for `XSPEC` fitting of BH masses M_{\bullet} lower than $1000 M_{\odot}$, because the pre-calculated library of disk spectra only extend to that BH mass limit. To model the high-/super-Eddington disk of a BH of $10^1 - 10^3 M_{\odot}$ mass scales, we modify `slimdz` by expanding the pre-calculated library down to $10 M_{\odot}$. We follow the same procedures in Wen et al. 2022 to calculate and ray-trace the disk spectrum given M_{\bullet} .

To have the new spectral library be consistent with the original library, we sample the $10^1 - 10^3 M_{\odot}$ mass range in the same way as the original $10^3 - 10^5 M_{\odot}$ mass range, simply scaling down all sampled values by two orders of magnitude. Then, for each sampled M_{\bullet} , we calculate the disk spectra for various mass accretion rates \dot{m} , inclinations θ , and BH spins a_{\bullet} . We use the same sampled values of \dot{m} , θ , and a_{\bullet} used to construct the original library in Wen et al. 2022.

Notably, when the disk is nearly face-on ($\theta < 3^{\circ}$), the ray-tracing does not behave well, as described in Psaltis & Johannsen 2011. Thus, to avoid errors and to keep the model self-consistent across different mass scales, we set the lower boundary of θ allowed in the modified `slimdz` to 3° . This is slightly larger than the limit of 2° in the original `slimdz` model for more massive BHs. The reason is that, for the lower mass BH range we consider here, the curvature is larger, aggravating the problems with near-face-on ray-tracing.

We note that in `slimdz` model, the viscosity parameter α (Shakura & Sunyaev 1973) is fixed to 0.1. Numerical simulations of super-Eddington accretion flows have shown that $\alpha \sim 0.1$ for a BH of $10 M_{\odot}$ and various \dot{m} (Sądowski et al. 2015). Furthermore, calculations indicate that the impact of α (0.01-0.1) on the emergent spectrum is small compared to that of other model parameters like M_{\bullet} or a_{\bullet} , across different M_{\bullet} scales (from 10 to $10^6 M_{\odot}$; e.g., Dotan & Shaviv 2011; Wen et al. 2020).

Meanwhile, although the disk radiative efficiency η is fixed to 0.1 in the `slimdz` model, it is do so only for the purpose of determining the unit of the mass accretion rate $\dot{m}_{\text{Edd}} = 1.37 \times 10^{21}$ kg s⁻¹ $(0.1/\eta)(M_{\bullet}/10^6 M_{\odot})$. The actual disk radiative efficiency can be determined from the physical value of \dot{m} after constraining the mass M_{\bullet} , and the efficiency can vary between epochs (as expected in the slim disk scenario when the \dot{m} changes; e.g., Abramowicz & Fragile 2013).

Moreover, Wen et al. 2022 ray-trace the accretion disk only up to $\leq 600 R_g$ (here $R_g = GM_{\bullet}/c^2$ is the gravitational radius of the BH), as regions with $R > 600 R_g$ are expected to contribute little to the X-ray flux of TDEs due to the significant temperature decrease as a function of radius. Wen et al. (2021) found that an error $\lesssim 1\%$ in flux is introduced by this choice of the outer disk radius for the ray-tracing. However, TDEs with smaller mass BHs are likely to have larger disks ($\gtrsim 2 \times 10^5 R_g$ for a $10 M_{\odot}$ BH disrupting a solar-type star), and such disks are quantitatively different from those with $\geq 10^4 M_{\odot}$ BHs. We test and find that, to keep the flux error $\lesssim 1\%$ for most prograde-spinning BHs, we have to perform the ray-tracing further to at least $800 R_g$ (Fig. A.1a). In the Appendix, we show the comparison between the disk spectra with different choices of outer radii for the ray-tracing. Therefore, in our model calculations, the disk is ray-traced up to $800 R_g$. We note that, in extreme cases of retrograde spinning BHs

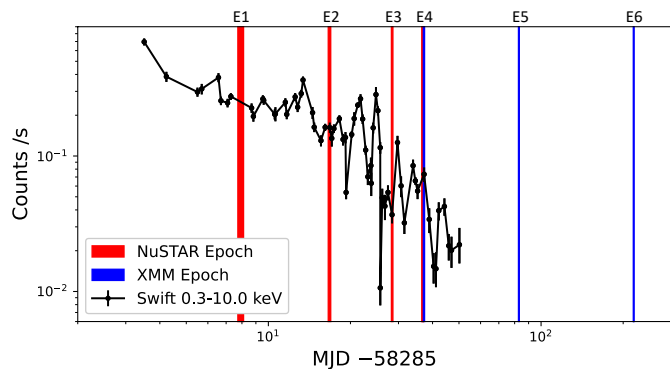


Fig. 1: *Swift* 0.3–10 keV light curve of AT2018cow. The time of the *NuSTAR* and *XMM-Newton* observations has been highlighted with red and blue vertical lines, respectively. The 6 epochs we use in this paper for grouping the observations and joint analysis are marked at the top of the figure. See Table B.1 for the details of the observations in each epoch. Note at E4, the *NuSTAR* and *XMM-Newton* observations do not overlap in time.

(e.g., $M_{\bullet} = 10 M_{\odot}$, $a_{\bullet} = -0.998$, and $\dot{m} = 100 \dot{m}_{\text{Edd}}$), the flux errors introduced by this choice of the ray-tracing radius could be as large as $\sim 50\%$ < 1 keV (Fig. A.1b). One should therefore be cautious when interpreting the results in those cases.

Recently, by combining thin-disk results at the innermost-stable-circular-orbit (ISCO) with numerical simulations, Mummery et al. 2024a finds that the disk plunging region inside the ISCO also contributes a significant part to the BH X-ray spectrum in some cases, associated with a finite stress at the ISCO due to a magnetic field and an extremely high spectral hardening factor of $f_c \sim 100$. In our case, the slim disk solution (e.g., temperature T and surface density Σ as a function of the disk radius r) describes the disk self-consistently from the event horizon to the outer disk edge (Sądowski et al. 2011; Wen et al. 2020). When constructing the `slimdz` spectra library, we employ an inner boundary at the ISCO for the ray-tracing purpose only. Wen et al. 2021 have tested and found that the flux difference in the 0.2–10 keV energy band between ray-tracing down to the horizon and down to the ISCO is nearly always $\lesssim 2\%$. Therefore, we conclude that the spectral impact of the disk plunging region is not significant in the slim disk cases of our interest, and for consistency we employ the ISCO as the inner boundary of the ray-tracing process in this paper as well.

4. Results

Fig. 1 shows the *Swift* 0.3–10.0 keV light curve, as well as the epochs of *NuSTAR* and *XMM-Newton* observations. We first explore the spectral characteristics by fitting the data with a fit function comprised of a power-law modified by the effects of Galactic extinction (the fit function in XSPEC’s syntax is `constant*TBabs*powerlaw`). Results show that, except for the first epoch, spectra from the other epochs can be well-fit by a power-law (C-stat/d.o.f. < 2 ; Table B.2). From Epoch 2 to 6, the source becomes increasingly softer in X-rays, with the power-law index changing from $\Gamma = 1.38 \pm 0.02$ (Epoch 2) to 2.8 ± 0.6

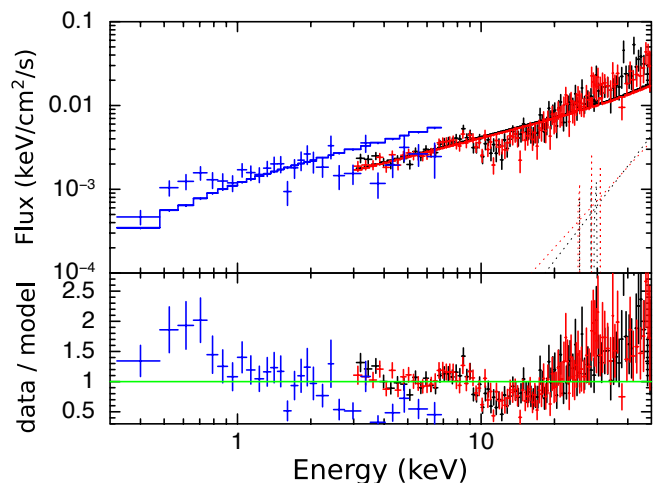


Fig. 2: The X-ray spectra from Epoch 1 fitted by a power-law model. In the upper panel we present the data, the power-law model (solid lines), and the background models (dotted lines). The blue, black, and red data are from *Swift*/XRT, *NuSTAR*/FPMA, and *NuSTAR*/FPMB, respectively. In the lower panel, we show the ratio between the observed number of counts (data) and the predicted number of counts in each spectral bin (model). Similar to what previous studies find, we observe X-ray features around ~ 6.4 keV and above 10 keV that are likely due to reflection.

(Epoch 6). The soft source spectrum at the latter epoch might indicate the appearance of a soft disk component in the energy range 0.3–1.5 keV.

From the fit residuals for Epoch 1 (Fig. 2), we confirm the X-ray features ~ 6.4 keV and $\gtrsim 10$ keV as found previously (Margutti et al. 2019). These features cause the source spectrum to be inconsistent with a single power-law fit function at Epoch 1, and they have been proposed to be due to the reflection of the primary power-law emission (possibly caused by a black hole corona or a jet base) off an accretion disk.

We then use the model `relxillCp` (Dauser et al. 2014; García et al. 2014; see also the references for a detailed description of each model parameter) to account for the disk reflection in the fit function. We note, in `relxillCp`, the disk is assumed to be a standard Shakura–Sunyaev thin disk (Shakura & Sunyaev 1973), and the incident power-law emission is modeled by `nthcomp` (Zdziarski et al. 1996), that assumes a multi-temperature black body seed spectrum modified by a Comptonising medium. Currently, there are no reflection models using a slim disk for the disk seed photons or calculating the GR effect, and so we use `relxillCp` to approximate the reflected emission off a slim disk (the total fit function in XSPEC’s syntax is `constant*TBabs*relxillCp`). Therefore, one should be cautious when interpreting the results from our fits with `relxillCp`. At Epoch 1, we find the source emission is consistent with `relxillCp`, i.e. an incident power-law-like emission plus a disk reflection (Table B.3). The Comptonising medium is constrained to be emitting a hard power-law ($\Gamma = 1.22 \pm 0.02$), and its electron temperature is constrained to be 28 ± 8 keV. The inclination constraint is $74^{\circ} \pm 2$ and the black hole spin constraint is 0.98 ± 0.01 .

We then test for the presence of a spectral component originating from an accretion disk in the other epochs of AT2018cow, using `slimdz`. Results are summarized in Table B.3. Among Epoch 2 to 6, we find that only for Epoch 4 the fit to the data is significantly improved by adding a disk component to the fit function (the total fit function in XSPEC's syntax is `"constant*TBabs*(powerlaw+slimdz)"`; $\Delta\text{AIC}=12.8$ compared to the power-law-only case, exceeds the very strong improvement threshold of 10; Akaike 1974); statistically, Epoch 2, 3, 5, and 6 require no disk components besides a simple power-law for reaching a good fit to the data. Meanwhile, a slim disk alone (`"constant*TBabs*slimdz"` in XSPEC's syntax) cannot describe the data well, for Epoch 2, 3, and 5. However, as the source becomes much softer at Epoch 6, we test and find that the source spectrum at this epoch is consistent with the slim disk model, yielding a black hole mass $\log(M_{\bullet}/M_{\odot})=2.3 \pm 0.9$, while due to data quality, other disk parameters are not well constrained (\dot{m} , θ , a_{\bullet}). The constraints on the black hole mass derived from the spectra both at Epoch 4 and at Epoch 6 are consistent with $\log(M_{\bullet}/M_{\odot}) \approx 2.4$.

Physically, it is likely that the accretion disk is present around the black hole not only at Epoch 1, 4, and 6, but also throughout the period (weeks) after the first detection (Epoch 1). At Epoch 2 and 3, the soft X-ray band (0.3–3.0 keV) can only be investigated through the *Swift*/XRT data. As the slim disk emits primarily soft X-rays, a lack of data of higher quality in the soft band, together with the presence of a strong power-law emission component, makes it impossible to constrain the disk emission at Epoch 2 and 3. At Epoch 4, however, the high quality 0.3–3.0 keV *XMM-Newton* data allows a significant measurement of this soft disk component. At Epoch 5, the general decrease in the source luminosity makes it impossible to detect the disk in the *XMM-Newton* observation especially since the source spectrum remains dominated by a power-law. At Epoch 6, although the luminosity keeps decreasing, we find the source spectrum has become much softer (Table B.2). It is likely that at this epoch the luminosity of the non-thermal component has diminished and the spectrum can be explained solely by the disk emission. The disk model fits the data well without the need of non-thermal components (Fig. 3).

Therefore, based on the results above, we assume the disk is present at all epochs and perform joint-fits combining the data from Epoch 2 to 6. The total fit function in XSPEC's syntax is `"constant*TBabs*(powerlaw+slimdz)"`. We force the disk parameter θ , M_{\bullet} and a_{\bullet} to be the same between epochs and fit their values, while we allow \dot{m} to vary between epochs and treat each \dot{m} as an individual fit parameter for each epoch. The power-law emission is also allowed to vary between epochs in our joint-fit. By jointly fitting Epoch 2 to 6, we find the black hole mass to be $\log(M_{\bullet}/M_{\odot})=2.4_{-0.1}^{+0.6}$, an upper limit to the inclination $\theta < 76^{\circ}$, and a broadly-constrained black hole spin $a_{\bullet} = 0.4_{-0.9}^{+0.5}$. We present the full list of parameter constraints from the joint-fit in Table B.4, and the ΔC -stat contour in $\{M_{\bullet}, a_{\bullet}\}$ space in Fig. 4.

The data at Epoch 4 and 6 plays a vital role in constraining the value of the BH mass. Nonetheless, it is important that we also consider the data at other epochs, because they will help us constrain parameters that might vary over the event and it can help us exclude models that are not consistent with the data (e.g., upper limits on the disk luminosity

can be derived). Notably, the inclination constraint derived from the thin-disk reflection model at Epoch 1 does not deviate from the slim disk results based on this joint-fit, while the thin-disk reflection model suggests a higher black hole spin than the slim disk results. The \dot{m} constraints are consistent with a scenario in which the accretion rate decreases from super-Eddington to sub-Eddington levels.

In all the fits above, we notice the re-normalization constant for *Swift* spectrum at Epoch 3 is constrained to be ~ 0.5 , which stands out from the re-normalization of *Swift* observations at other epochs. We manually check the CCD image for this particular *Swift* observation and find a stripe of dead pixels to be present in the source extraction region. We also checked the other *Swift* data and find this row of dead pixels to lie away from the source extraction region. This defect on the CCD leads to a loss in the instrumental effective area and thus results in a decrease of the number of counts in this particular spectrum, explaining the lower constant in the joint-fit of the *Swift* spectra with those of the other satellite data.

5. Discussion

By analyzing AT2018cow data from *Swift*, *NuSTAR*, and *XMM-Newton*, we find that starting from Epoch 2 the source's X-ray spectrum can be interpreted as originating from a slim disk plus a non-thermal spectral component modeled by a power-law. For the X-ray spectral fits, we extend the black hole mass range available for the slim disk model `slimdz` (Wen et al. 2022) from $10^3 - 10^6 M_{\odot}$ to the black hole mass range $10^1 - 10^6 M_{\odot}$. This extension to the model `slimdz` is now publicly available² to be used in XSPEC. We confirm that AT2018cow's X-ray spectrum during Epoch 1 can be well-described by a disk reflection model as was reported before (Margutti et al. 2019). When the source becomes softer in X-rays after $\gtrsim 200$ days, the source spectrum becomes consistent with the emission from a slim disk. From the slim disk modeling, an IMBH of mass $\log(M_{\bullet}/M_{\odot})=2.4_{-0.1}^{+0.6}$ (at 68% confidence level) is derived for the mass of the central compact object, while the disk inclination ($\theta < 76^{\circ}$) and the BH spin ($a_{\bullet} = 0.4_{-0.9}^{+0.5}$) are less strongly constrained (see Table B.4 for all the parameter constraints). All the parameter constraints are derived under the assumption that the disk viscosity parameter $\alpha = 0.1$. Our spectral modeling shows that the X-ray spectrum becomes softer at late time due to the disappearance of the non-thermal spectral component in concert with a decrease in the mass accretion rate, \dot{m} . The \dot{m} values derived from our spectral fit are consistent with a decrease from super- to sub-Eddington levels at late-times.

Our independent mass measurement of AT2018cow is consistent with several mass constraints available in the literature based on energetic arguments, late-time UV data modeling, and X-ray timing assumptions (Pasham et al. 2022; Migliori et al. 2023; Inkenhaag et al. 2023). The mass constraint $\log(M_{\bullet}/M_{\odot})=2.4_{-0.1}^{+0.6}$ confirms the presence of an accreting IMBH as the central compact object. Such an IMBH can be formed through the accretion of gas onto a seed stellar-mass BH (which can take cosmic timescales; e.g., Madau & Rees 2001; Greif et al. 2011), or through the direct collapse of pristine gas clouds in the early Universe (e.g., Loeb & Rasio 1994; Bromm &

² 10.5281/zenodo.11110331

Loeb 2003; Lodato & Natarajan 2006), or through the BH merger events (e.g., Abbott et al. 2016). The direct mass measurement from the slim disk modeling demonstrates a possible new way to study other AT2018cow-like LFBOs that are also accompanied by variable X-ray emission (e.g., AT2020xnd/ZTF20acigmel, Ho et al. 2022a; Bright et al. 2022; AT2020rmf, Yao et al. 2022).

An IMBH nature for AT2018cow is in line with scenarios that involve an accreting central compact object (e.g., TDE; Kuin et al. 2019; Perley et al. 2019; BH–star binary merger; Metzger 2022). Particularly, for the IMBH–TDE scenario, we estimate the late-time disk outer radius to be $\approx 13 R_{\odot}$ given an IMBH of mass $10^{2.4} \approx 250 M_{\odot}$ disrupting a solar-mass star³. Thus, the predicted radius from the IMBH–TDE scenario is similar to that from the binary merger scenario (15–40 R_{\odot} ; Migliori et al. 2023) and has the same order of magnitude as values derived from the late-time UV observations ($\approx 40 R_{\odot}$; Inkenhaag et al. 2023; Migliori et al. 2023). Meanwhile, in the core-collapse scenario, the fall-back stellar ejecta typically forms a much smaller disk, and this generally leads to an outer disk radius of $\sim 10^{-3} R_{\odot}$ at late times (Migliori et al. 2023). Besides the outer disk radius, other parameters might also differ among scenarios, e.g., the peak \dot{m} . We refer to previous studies for a quantitative discussion of how those parameters depend on the BH mass in different scenarios (e.g., Metzger 2022; Migliori et al. 2023).

In our study, the non-thermal spectral component is modeled by a power-law component. Possible origins of the power-law component include a Comptonising medium (BH corona) up-scattering the disk photons, similar to that found in other BH accretion systems like X-ray binaries or Active Galactic Nuclei (AGNs) (e.g., Esin et al. 1997; Nowak et al. 2011). It is also possible that some of the non-thermal emission is generated by shock interactions with the circumstellar material (CSM; e.g., Rivera Sandoval et al. 2018; Margutti et al. 2019; Fox & Smith 2019; Leung et al. 2020. Interestingly, when the accretion rate becomes sub-Eddington at late times, we find the non-thermal emission diminishes and the X-ray spectrum can be well-fit by a slim disk model. Spectral state transitions involving a varying non-thermal spectral component has also been observed in several TDE systems (e.g., Bade et al. 1996; Komossa et al. 2004; Wevers et al. 2019; Jonker et al. 2020; Wevers et al. 2021; Cao et al. 2023).

In AT2018cow, there is evidence for a dense CSM (Ho et al. 2019). Theoretical work shows that a dense CSM can be present in both a TDE scenario (Linial & Quataert 2024), where the dense CSM is produced by the outflows from the BH–star mass transfer prior to the full stellar disruption, and in a binary merger scenario, where the dense CSM is produced in the common envelope phase between a stellar-mass BH (1–20 M_{\odot}) and its massive stellar companion (Metzger 2022). At present, it is unclear if this latter model can be extrapolated to accommodate a BH of $\approx 250 M_{\odot}$, the value suggested by our work. If that

³ While the `slimdz` model limits the disk outer radius to $\leq 800 R_g$ (for ray-tracing purposes; see Section 3), in the case of AT2018cow, we estimate an error on the flux of $\lesssim 0.5\%$ introduced to the model below 1 keV by this choice of disk radius (Fig. A.1c). Meanwhile, the actual disk radius is estimated by assuming a typical TDE disk, whose outer radius is about twice the tidal radius: $R_{\text{out}} \approx 2R_t = 2R_{\text{star}}(M_{\bullet}/M_{\text{star}})^{1/3}$ (e.g., Rees 1988; Kochanek 1994). See also the Appendix.

extrapolation is plausible, our BH mass determination of AT2018cow is consistent with both the TDE and BH–star merger scenarios.

Since no reflection models for the reflected emission from a slim disk are available, in our analysis, the reflection features (i.e., the broadened iron $K\alpha$ line ~ 6.4 keV and the Compton hump >10 keV) dominating the first *NuSTAR* epoch (and not detected in all later epochs) are modeled by disk reflection `relxillCp` (Dauser et al. 2014; García et al. 2014). The model `relxillCp` assumes that a standard thin disk reflects the emission from a Comptonising medium with an incident power-law spectral shape. Given the same Comptonising medium, the geometrical differences between the thin and the slim disks will result in differences in the emissivity profile of the reflected emission. This inconsistency between the likely super-Eddington accretion and the thin-disk assumption at Epoch 1 might contribute to the different spin constraints derived from the thin-disk ($a_{\bullet} = 0.98 \pm 0.01$) and the slim-disk ($a_{\bullet} = 0.4_{-0.9}^{+0.5}$) results. Despite that, we notice the inclination constraint from `relxillCp` ($\theta = 74^{\circ} \pm 2$) is in general agreement with the value derived from the slim disk modeling using data from all later epochs ($< 76^{\circ}$). The material that is responsible for the reflected emission can involve the rapidly expanding outflow. Its density will decrease with time, which leads to the diminishing of reflection features in later epochs (e.g., Margutti et al. 2019).

While we extend the pre-calculated library of the disk spectra in `slimdz` to model the disk of $M_{\bullet} < 1000 M_{\odot}$, there exists a slim disk model `slimbh` (Sądowski et al. 2011; Straub et al. 2011) that is available for the disk luminosity $L_{\text{disk}} \leq 1.25 L_{\text{Edd}}$ (with L_{disk} as one of the fit parameters in `slimbh`, and $L_{\text{Edd}} \equiv 1.26 \times 10^{38} (M/M_{\odot}) \text{ erg/s}$)⁴. Physically, compared to `slimbh`, the `slimdz` model includes the loss of angular momentum due to radiation at each disk annulus. This adjustment alters the predicted effective temperature of the inner disk region, especially for high-spin, low-accretion disks (Wen et al. 2021). Moreover, a different estimate of the disk spectral hardening factor f_c (Davis & El-Abd 2019) is employed by `slimdz` compared with `slimbh`.

We compare the results derived by using `slimdz` with those obtained using `slimbh` by jointly fitting Epoch 2 to 6 with the fit function "`constant*TBabs*(powerlaw+slimbh)`", and comparing the results (presented in Table B.5) to the those obtained with `slimdz` (Table B.4). Both disk models provide a good fit to the combined data from Epoch 2 to 6. The mass constraint derived from `slimbh` is slightly higher ($\log(M_{\bullet}/M_{\odot}) = 3.2 \pm 0.2$) although marginally consistent with that in the `slimdz` case ($\log(M_{\bullet}/M_{\odot}) = 2.4_{-0.1}^{+0.6}$). Besides the physical differences between the disk models, it is possible that when fitting the super-Eddington spectra at Epoch 4, the upper parameter range of $L_{\text{disk}}/L_{\text{Edd}} \leq 1.25$ in `slimbh` limits the lower boundary of the mass constraint (since for a given observed luminosity, $L_{\text{disk}}/L_{\text{Edd}} \propto 1/M_{\bullet}$). In this sense, as $L_{\text{disk}}/L_{\text{Edd}}$ at Epoch 4 is constrained to be >1.0 and is limited by the parameter range of ≤ 1.25 , the lower boundary of the mass constraint derived from `slimbh` is underestimated, causing the mass constraints between

⁴ Note in `slimdz`, instead of L_{disk} , \dot{m} in the unit of $\dot{M}_{\text{Edd}} \equiv 1.37 \times 10^{15} (M/M_{\odot}) \text{ kg/s}$ is used to solve the disk equations that determines the disk luminosity in erg/s.

the two disk models to be just marginally consistent in Table B.4 and Table B.5. Indeed, the mass constraints derived from both disk models are consistent when jointly fitting Epoch 5 and 6 (Table B.6), at which two epochs the disk is likely at sub-Eddington accretion levels. We also test the $\alpha = 0.01$ cases in the `slimbh` model. The fit results with $\alpha = 0.01$ do not differ from those with $\alpha = 0.1$ shown in Table B.5 and B.6 (for `slimbh` cases). This test suggests that the choice of $\alpha = 0.1$ does not significantly affect the slim disk spectrum or the BH mass constraint, though the spectral library for `slimdz` does not currently extend to lower α values. For the above reason concerning the upper limit of $L_{\text{disk}}/L_{\text{Edd}}$, and due to the improved treatment of the angular momentum transport by radiation `slimdz` mentioned above, we prefer the results derived from `slimdz` (Table B.4).

6. Conclusions

We have performed X-ray spectral analysis on *NuSTAR*, *Swift*, and *XMM-Newton* data of the LFBOT AT2018cow and find evidence for an accretion disk soon after the source's discovery. Based on slim disk modeling, we constrain the mass of the central compact object to be $\log(M_{\bullet}/M_{\odot}) = 2.4_{-0.1}^{+0.6}$ at the 68% confidence level. Our mass measurement is independent from, but consistent with, the results from previously employed methods. Therefore, we provide further evidence for an accreting intermediate-mass black hole (10^2 – $10^6 M_{\odot}$) as the central compact object residing in AT2018cow, and by extension, in similar LFBOT sources. The mass constraint is consistent with both the tidal disruption and the black hole–star merger scenarios, if the latter model can be extrapolated to the measured black hole mass.

Our results are consistent with the scenario in which the source accretion rate decreases from super-Eddington to sub-Eddington levels ~ 200 days after its discovery. We find the late-time spectrum to be softer compared to the early-time spectra, consistent with emission from a slim disk at sub-Eddington accretion levels. In our analysis, a modified version of the existing slim disk model `slimdz` is used to model the high-/super-Eddington disk of a black hole at mass scales of 10 to 1000 M_{\odot} . Through this work, we demonstrate a possible new way of studying LFBOT sources that have X-ray emission similar to AT2018cow.

Acknowledgements. We thank the referee for comments that helped to improve this manuscript. This work used the Dutch national e-infrastructure with the support of the SURF Cooperative using grant no. EINF-3954. This work made use of data supplied by the UK Swift Science Data Centre at the University of Leicester. P.G.J. has received funding from the European Research Council (ERC) under the European Union's Horizon 2020 research and innovation programme (Grant agreement No. 101095973). AIZ acknowledges support in part from grant NASA ADAP #80NSSC21K0988 and grant NSF PHY-2309135 to the Kavli Institute for Theoretical Physics (KITP).

Data Availability

All the X-ray data in this paper are publicly available from the HEASARC data archive (<https://heasarc.gsfc.nasa.gov/>). A reproduction package is available at DOI: 10.5281/zenodo.11110331. The extension to the `slimdz` model used in this paper is available at 10.5281/zenodo.11110331.

References

- Abbott, B. P., Abbott, R., Abbott, T., et al. 2016, PRL, 116, 241102
Abramowicz, M., Czerny, B., Lasota, J., & Szuszkiewicz, E. 1988, ApJ, 332, 646
Abramowicz, M. A. & Fragile, P. C. 2013, Living Reviews in Relativity, 16, 1
Adelman-McCarthy, J. K., Agüeros, M. A., Allam, S. S., et al. 2008, ApJ Suppl, 175, 297
Akaïke, H. 1974, IEEE transactions on automatic control, 19, 716
Arcavi, I., Wolf, W. M., Howell, D. A., et al. 2016, ApJ, 819, 35
Arnaud, K. 1996, in Astronomical Data Analysis Software and Systems V, Vol. 101, 17
Bade, N., Komossa, S., & Dahlem, M. 1996, A&A, 309, L35
Bright, J. S., Margutti, R., Matthews, D., et al. 2022, ApJ, 926, 112
Bromm, V. & Loeb, A. 2003, ApJ, 596, 34
Cao, Z., Jonker, P., Wen, S., Stone, N., & Zabludoff, A. 2023, MNRAS, 519, 2375
Cash, W. 1979, ApJ, 228, 939
Coppejans, D. L., Margutti, R., Terreran, G., et al. 2020, ApJL, 895, L23
Dauser, T., García, J., Parker, M., Fabian, A., & Wilms, J. 2014, MNRAS Letters, 444, L100
Davis, S. W. & El-Abd, S. 2019, ApJ, 874, 23
Dotan, C. & Shaviv, N. J. 2011, MNRAS, 413, 1623
Drout, M. R., Chornock, R., Soderberg, A. M., et al. 2014, ApJ, 794, 23
Esin, A. A., McClintock, J. E., & Narayan, R. 1997, ApJ, 489, 865
Evans, P., Beardmore, A., Page, K., et al. 2009, MNRAS, 397, 1177
Fox, O. D. & Smith, N. 2019, MNRAS, 488, 3772
García, J., Dauser, T., Lohfink, A., et al. 2014, ApJ, 782, 76
Gottlieb, O., Tchekhovskoy, A., & Margutti, R. 2022, MNRAS, 513, 3810
Greif, T. H., Springel, V., White, S. D., et al. 2011, ApJ, 737, 75
Harrison, F. A., Boggs, S., Christensen, F., et al. 2010, in Space Telescopes and Instrumentation 2010: Ultraviolet to Gamma Ray, Vol. 7732, SPIE, 189–196
Ho, A. Y., Margalit, B., Bremer, M., et al. 2022a, ApJ, 932, 116
Ho, A. Y., Perley, D. A., Gal-Yam, A., et al. 2023, ApJ, 949, 120
Ho, A. Y., Perley, D. A., Yao, Y., et al. 2022b, ApJ, 938, 85
Ho, A. Y., Phinney, E. S., Ravi, V., et al. 2019, ApJ, 871, 73
Inkenhaag, A., Jonker, P. G., Levan, A. J., et al. 2023, MNRAS, 525, 4042
Jonker, P., Stone, N., Generozov, A., van Velzen, S., & Metzger, B. 2020, ApJ, 889, 166
Kaastra, J. & Bleeker, J. 2016, A&A, 587, A151
Katayama, H., Takahashi, I., Ikebe, Y., Matsushita, K., & Freyberg, M. 2004, A&A, 414, 767
Kochanek, C. S. 1994, Astrophysical Journal, Part 1 (ISSN 0004-637X), vol. 422, no. 2, p. 508-520, 422, 508
Komossa, S., Halpern, J., Scharrel, N., et al. 2004, ApJL, 603, L17
Kuin, N. P. M., Wu, K., Oates, S., et al. 2019, MNRAS, 487, 2505
Leung, S.-C., Blinnikov, S., Nomoto, K., et al. 2020, ApJ, 903, 66
Leung, S.-C., Fuller, J., & Nomoto, K. 2021, ApJ, 915, 80
Linial, I. & Quataert, E. 2024, arXiv preprint arXiv:2407.00149
Lodato, G. & Natarajan, P. 2006, MNRAS, 371, 1813
Loeb, A. & Rasio, F. A. 1994, ApJ, 432, 52
Madau, P. & Rees, M. J. 2001, ApJL, 551, L27
Margutti, R., Metzger, B., Chornock, R., et al. 2019, ApJ, 872, 18
Metzger, B. D. 2022, ApJ, 932, 84
Migliori, G., Margutti, R., Metzger, B., et al. 2023, ApJL accepted; arXiv preprint arXiv:2309.15678
Mohan, P., An, T., & Yang, J. 2020, ApJL, 888, L24
Mummery, A. & Balbus, S. A. 2020, MNRAS, 492, 5655
Mummery, A., Ingram, A., Davis, S., & Fabian, A. 2024a, MNRAS, 531, 366
Mummery, A., van Velzen, S., Nathan, E., et al. 2024b, MNRAS, 527, 2452
Nayana, A. & Chandra, P. 2021, ApJL, 912, L9
Nowak, M. A., Hanke, M., Trowbridge, S. N., et al. 2011, ApJ, 728, 13
Pagani, C., Morris, D., Racusin, J., et al. 2007, in UV, X-Ray, and Gamma-Ray Space Instrumentation for Astronomy XV, Vol. 6686, SPIE, 80–88
Pasham, D. R., Ho, W. C., Alston, W., et al. 2022, Nature Astronomy, 6, 249
Pellegrino, C., Howell, D., Vinkó, J., et al. 2022, ApJ, 926, 125
Perley, D. A., Ho, A. Y., Yao, Y., et al. 2021, MNRAS, 508, 5138
Perley, D. A., Mazzali, P. A., Yan, L., et al. 2019, MNRAS, 484, 1031
Prentice, S., Maguire, K., Smartt, S., et al. 2018, ApJL, 865, L3

- Psaltis, D. & Johannsen, T. 2011, *ApJ*, 745, 1
- Pursiainen, M., Childress, M., Smith, M., et al. 2018, *MNRAS*, 481, 894
- Rees, M. J. 1988, *Nature*, 333, 523
- Rest, A., Garnavich, P. M., Khatami, D., et al. 2018, *Nature Astronomy*, 2, 307
- Rivera Sandoval, L., MacCarone, T., Corsi, A., et al. 2018, *MNRAS Letters*, 480, L146
- Sądowski, A., Abramowicz, M., Bursa, M., et al. 2011, *A&A*, 527, A17
- Sądowski, A., Narayan, R., Tchekhovskoy, A., et al. 2015, *MNRAS*, 447, 49
- Shakura, N. I. & Sunyaev, R. A. 1973, *A&A*, 24, 337
- Smartt, S., Clark, P., Smith, K., et al. 2018, *ATel*, 11727, 1
- Straub, O., Bursa, M., Sa, A., et al. 2011, *A&A*, 533, A67
- Tampo, Y., Tanaka, M., Maeda, K., et al. 2020, *ApJ*, 894, 27
- Tanaka, M., Tominaga, N., Morokuma, T., et al. 2016, *ApJ*, 819, 5
- van Velzen, S., Stone, N. C., Metzger, B. D., et al. 2019, *ApJ*, 878, 82
- Wen, S., Jonker, P. G., Stone, N. C., Van Velzen, S., & Zabludoff, A. I. 2023, *MNRAS*, 522, 1155
- Wen, S., Jonker, P. G., Stone, N. C., & Zabludoff, A. I. 2021, *ApJ*, 918, 46
- Wen, S., Jonker, P. G., Stone, N. C., Zabludoff, A. I., & Cao, Z. 2022, *ApJ*, 933, 31
- Wen, S., Jonker, P. G., Stone, N. C., Zabludoff, A. I., & Psaltis, D. 2020, *ApJ*, 897, 80
- Wen, S., Wang, S., & Luo, X. 2018, *JCAP*, 2018, 011
- Wevers, T., Pasham, D. R., van Velzen, S., et al. 2021, *ApJ*, 912, 151
- Wevers, T., Stone, N. C., van Velzen, S., et al. 2019, *MNRAS*, 487, 4136
- Wilms, J., Allen, A., & McCray, R. 2000, *ApJ*, 542, 914
- Yao, Y., Ho, A. Y., Medvedev, P., et al. 2022, *ApJ*, 934, 104
- Zdziarski, A. A., Johnson, W. N., & Magdziarz, P. 1996, *MNRAS*, 283, 193
- Zhang, W., Shu, X., Chen, J.-H., et al. 2022, *Research in Astronomy and Astrophysics*, 22, 125016

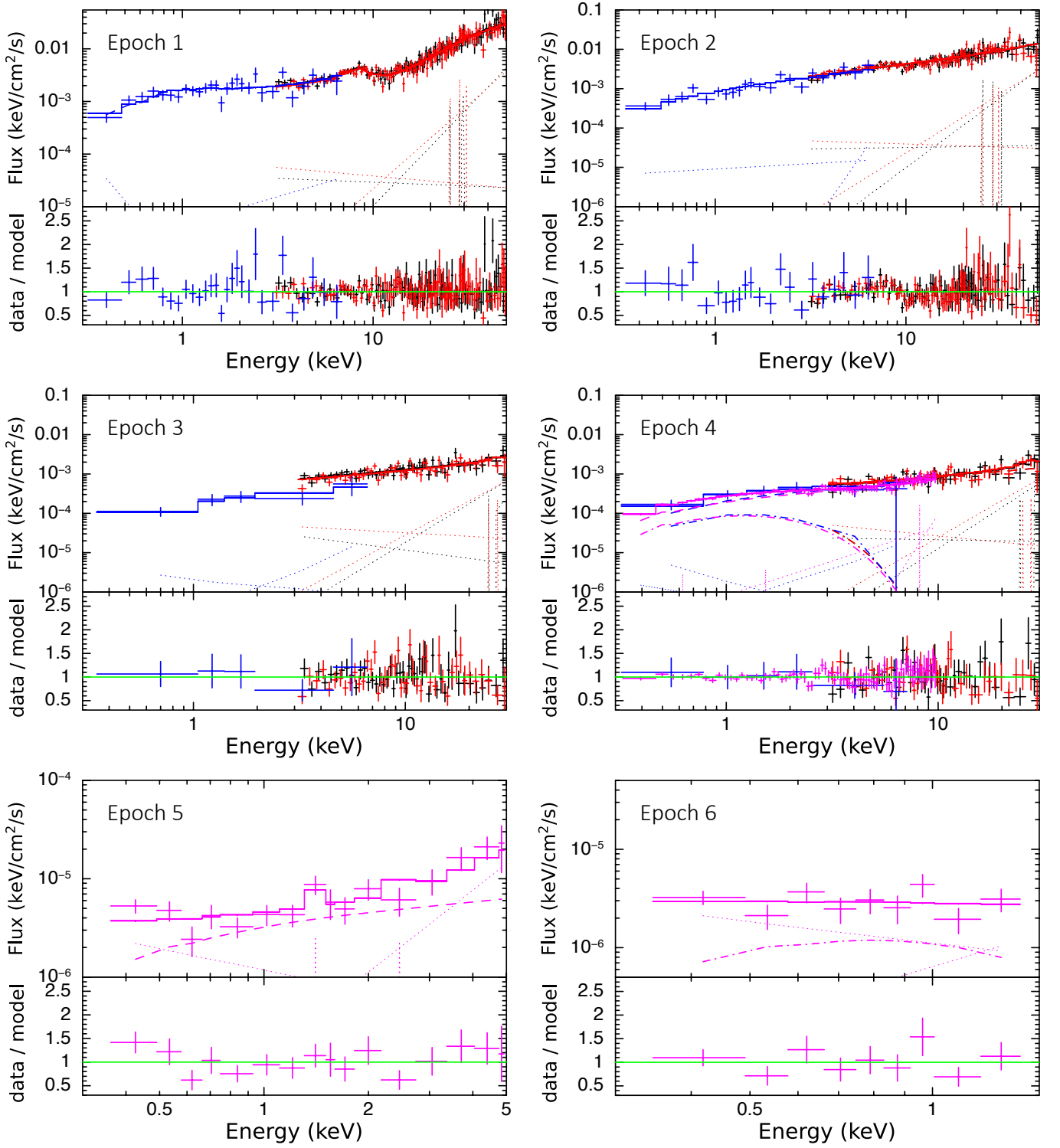


Fig. 3: The best-fit results based on the spectral analysis presented in Table B.3. For each figure, in the upper panel we present the spectrum as well as the best-fit models, and in the lower panel we present the ratio between the observed number of counts (data) and the best-fit predicted number of counts in each spectral bin (model). In all figures, the solid, dashed, dot-dashed, and dotted lines represent the best-fit source+background model, the power-law spectral component, the slim disk component, and the background models, respectively; the blue, black, red, and magenta data are from *Swift*/XRT, *NuSTAR*/FPMA, *NuSTAR*/FPMB, and *XMM-Newton*/EPIC-pn, respectively. Notice the y-axes in the upper panels of each figure are different in scales for illustration purpose.

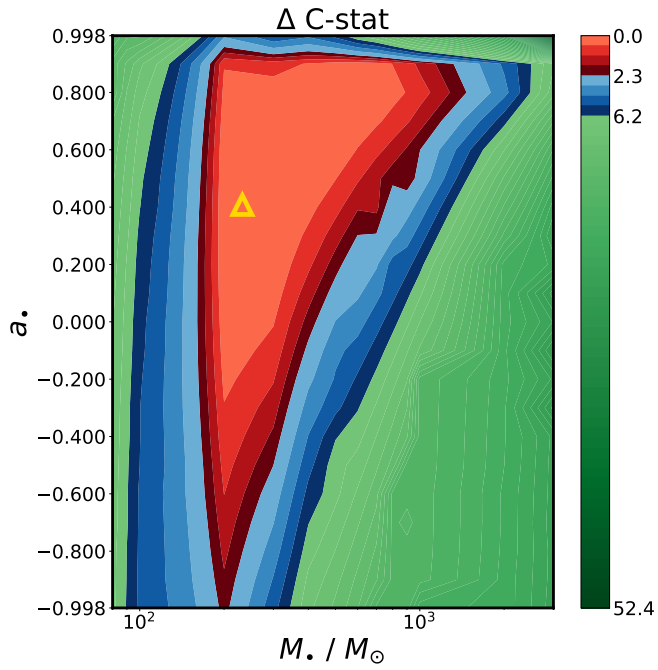


Fig. 4: Constraints on M_{\bullet} and a_{\bullet} based on a joint fit of the X-ray spectra from Epoch 2 to 6 with the slim disk model (Table B.4). We calculate the $\Delta C\text{-stat}$ across the $\{M_{\bullet}, a_{\bullet}\}$ plane. The best-fit point with the lowest C-stat is marked by the yellow triangle. Areas within 1σ and 2σ confidence levels are filled by red and blue colours, respectively. At 1σ for the two-parameter fits, M_{\bullet} is constrained to be $\log(M_{\bullet}/M_{\odot}) = 2.4^{+0.6}_{-0.1}$, while a_{\bullet} is virtually unconstrained.

Appendix A: The choice of the outer disk radius in `slimdz`

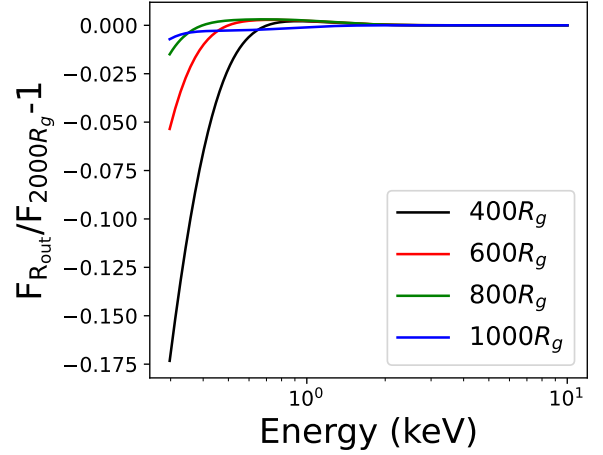
For a $10 M_{\odot}$ BH disrupting a solar-type star, the TDE disk radius could be well above $1 \times 10^5 R_g$. However, the regions $\geq 10^3 R_g$ contribute little to the X-ray flux, since the disk temperature decreases with radius. It is orders-of-magnitude lower for $\geq 10^3 R_g$ compared to the innermost disk region (e.g., Straub et al. 2011; Sądowski et al. 2011). As it is computationally too expensive to ray-trace the whole disk, when constructing the spectral library for `slimdz`, we set a fixed value of the outer disk radius R_{out} , and do not ray-trace the disk region further than R_{out} . Wen et al. 2021 estimate a flux error of $\lesssim 1\%$ when choosing $R_{\text{out}} = 600 R_g$ for a $10^4 M_{\odot}$ BH. Here we test different choices of R_{out} when ray-tracing the slim disk around a $10 M_{\odot}$ BH.

We consider a $10 M_{\odot}$, non-spinning BH with $\dot{m} = \dot{m}_{\text{Edd}}$, observed at an inclination of 45° . Fig. A.1a shows the relative flux differences between different R_{out} choices. The relative flux error is $\lesssim 1\%$ when $R_{\text{out}} > 800 R_g$. For higher M_{\bullet} , higher a_{\bullet} , and lower \dot{m} , the flux difference would be smaller, as the innermost disk region becomes more dominant compared to the outer disk region. Therefore, in the main text, we produce the spectral library of `slimdz` with $R_{\text{out}} = 800 R_g$, accelerating the calculation while the flux error is minimal.

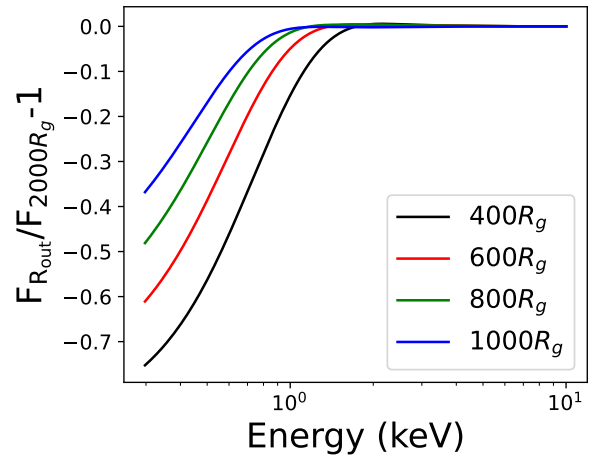
Note that a choice of $R_{\text{out}} = 800 R_g$ could introduce larger flux errors for a lower a_{\bullet} or for a higher \dot{m} . In extreme cases, e.g., $M_{\bullet} = 10 M_{\odot}$, $a_{\bullet} = -0.998$, $\dot{m} = 100 \dot{m}_{\text{Edd}}$, the flux error could be as large as $\sim 50\%$ (Fig. A.1b). Therefore, one should be cautious when modeling a retrograde stellar-mass BH and a disk of large \dot{m} with the currently available `slimdz` model.

Lastly, we estimate the flux error imposed by the choice of $R_{\text{out}} = 800 R_g$, in the particular case of AT2018cow. We consider the case of $M_{\bullet} = 250 M_{\odot}$, $a_{\bullet} = 0.4$, $\dot{m} = 5 \dot{m}_{\text{Edd}}$, and $\theta = 74^\circ$ (as derived from the `slimdz` disk modeling in Table B.4). We find a relative flux error of $\lesssim 0.5\%$ with $R_{\text{out}} = 800 R_g$ (Fig. A.1c).

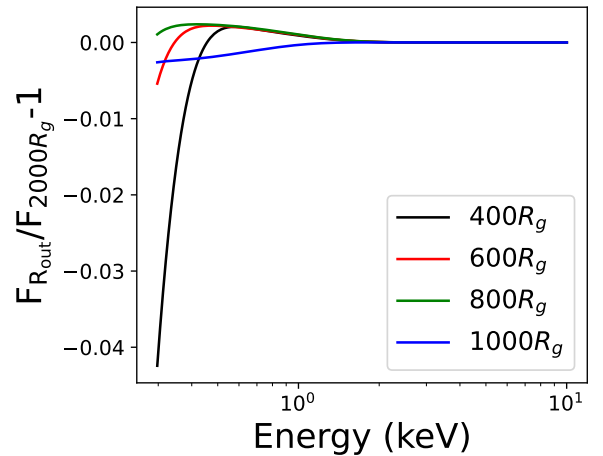
Appendix B: Tables



(a) $M_{\bullet} = 10 M_{\odot}$, $a_{\bullet} = 0$, $\dot{m} = \dot{m}_{\text{Edd}}$, $\theta = 45^\circ$



(b) $M_{\bullet} = 10 M_{\odot}$, $a_{\bullet} = -0.998$, $\dot{m} = 100 \dot{m}_{\text{Edd}}$, $\theta = 45^\circ$



(c) $M_{\bullet} = 250 M_{\odot}$, $a_{\bullet} = 0.4$, $\dot{m} = 5 \dot{m}_{\text{Edd}}$, $\theta = 74^\circ$

Fig. A.1: Here we investigate the effect of different choice of the outer disk radius R_{out} for the ray-tracing, on the emergent disk spectrum. The relative error is calculated as $\frac{F_{R_{\text{out}}} - F_{2000R_g}}{F_{2000R_g}}$. F_r denotes the X-ray flux calculated with $R_{\text{out}} = r$. We use F_{2000R_g} as the reference spectrum, as regions beyond $2000 R_g$ do not produce significant X-ray emissions due to the disk temperature decreasing as a function of radius. In the last test (bottom-middle), values of the disk parameters are similar to our best-fit results for AT2018cow (Table B.4).

Table B.1: Journal listing properties of the observations analyzed in this paper.

Epoch	Satellite	ObsID(Label)	Date	Exposure (ks)	R_{circ} (")	Energy band (keV)
Epoch 1	<i>NuSTAR</i>	90401327002	2018-06-23	32.4	30	3.0-50.0 keV
	<i>Swift</i>	00010724012	2018-06-23	2.5	59	0.3-7.0
		00010724013	2018-06-23			
		00010724010	2018-06-23			
Epoch 2	<i>NuSTAR</i>	90401327004	2018-07-02	30.0	30	3.0-50.0
	<i>Swift</i>	00010724046	2018-07-02	2.5	59	0.3-7.0
		00010724047	2018-07-02			
		00010724048	2018-07-02			
Epoch 3	<i>NuSTAR</i>	90401327006	2018-07-14	31.2	30	3.0-30.0
	<i>Swift</i>	00088782001	2018-07-14	2.2	35.4	0.3-7.0
Epoch 4	<i>NuSTAR</i>	90401327008	2018-07-22	32.9	30''	3.0-30.0
	<i>Swift</i>	00010724087	2018-07-21	1.6	35.4	0.3-7.0
		<i>XMM-Newton</i>	0822580401	2018-07-23	33.0	25
Epoch 5	<i>XMM-Newton</i>	0822580501	2018-09-06	45.0	25	0.3-5.0
Epoch 6	<i>XMM-Newton</i>	0822580601	2019-01-20	56.4	25	0.3-1.5

Notes. We group all observations by time into 6 epochs and fit the data in each epoch simultaneously. *Swift* observations within the same epoch are combined and treated as a single observation. We also give the radius of the circular region that we use for the source+background spectral extraction in each observation (R_{circ}). We followed Evans et al. (2009) in determining the radius of this source+background region to extract for *Swift* observations. In our spectral analysis, the energy band we use is given in the last column.

Table B.2: Parameter constraints from fitting the data within each epoch with a power-law model.

Model	Parameter	Epoch 1	Epoch 2	Epoch 3	Epoch 4	Epoch 5	Epoch 6
Constant	C_{FPMA}				[1.0]		
	C_{FPMB}	-	1.01 ± 0.03	0.92 ± 0.04	1.00 ± 0.06	-	-
	C_{Swift}	-	0.95 ± 0.07	0.47 ± 0.08	0.9 ± 0.1	-	-
	$C_{\text{XMM-Newton}}$	-	-	-	0.78 ± 0.04	-	-
TBabs	N_{H} (10^{20} cm^{-2})				[5.0]		
powerlaw	Γ	-	1.38 ± 0.02	1.52 ± 0.05	1.68 ± 0.01	1.7 ± 0.2	2.4 ± 0.7
	norm ($\text{keV}^{-1} \text{cm}^{-2} \text{s}^{-1}$)	-	$(10.0 \pm 0.5) \times 10^{-4}$	$(4.2 \pm 0.4) \times 10^{-4}$	$(3.9 \pm 0.2) \times 10^{-4}$	$(3.7 \pm 0.4) \times 10^{-6}$	$(1.2 \pm 0.4) \times 10^{-6}$
	C-stat/d.o.f.	-	256.8/267	174.0/158	221.0/231	47.0/33	12.0/9

Notes. We use a constant model to account for differences in normalization between each instrument and fix the constant for *NuSTAR*/*FPMA* spectra $C_{\text{FPMA}} = 1$ in each epoch. The total fit function is thus "**constant*TBabs*powerlaw**". Parameter values held fixed during the fit are given inside square brackets. No parameter constraints are given for Epoch 1, because at this epoch the source X-rays are dominated by reflection. With time the source spectrum seems to become softer.

Table B.3: Parameter constraints from our spectral analysis, with a fit function of "constant*TBabs*relxillCp" for Epoch 1, and a fit function of "constant*TBabs*(powerlaw+slimd)" for Epoch 2 to 6.

Model	Parameter	Epoch 1	Epoch 2	Epoch 3	Epoch 4	Epoch 5	Epoch 6
Constant	C_{FPMB}	0.96 ± 0.02	1.01 ± 0.03	0.92 ± 0.04	1.00 ± 0.06	-	-
	C_{Swift}	1.00 ± 0.06	0.95 ± 0.07	0.47 ± 0.08	0.9 ± 0.1	-	-
	$C_{\text{XMM-Newton}}$	-	-	-	0.79 ± 0.04	-	-
TBabs	$N_{\text{H}} (10^{20} \text{ cm}^{-2})$	[5.0]					
powerlaw	Γ	-	1.38 ± 0.02	1.52 ± 0.05	1.52 ± 0.05	1.7 ± 0.2	-
	norm ($\text{keV}^{-1} \text{cm}^{-2} \text{s}^{-1}$)	-	$(10.0 \pm 0.5) \times 10^{-4}$	$(4.2 \pm 0.4) \times 10^{-4}$	$(2.8 \pm 0.4) \times 10^{-4}$	$(3.7 \pm 0.4) \times 10^{-6}$	-
slimd	$\dot{m} (\dot{m}_{\text{Edd}})$	-	-	-	>0.5	-	<4.0
	$\theta (^{\circ})$	-	-	-	<81	-	NC
	$\log(M_{\bullet}/M_{\odot})$	-	-	-	$2.4_{-0.2}^{+0.8}$	-	2.3 ± 0.9
	a_{\bullet}	-	-	-	>-0.6	-	NC
relxillCp	$\theta (^{\circ})$	74 ± 2	-	-	-	-	-
	a_{\bullet}	0.98 ± 0.01	-	-	-	-	-
	kT_e (keV)	28 ± 8	-	-	-	-	-
	Γ	1.22 ± 0.02	-	-	-	-	-
	q	4 ± 2	-	-	-	-	-
	$\log(\xi)$	3.45 ± 0.06	-	-	-	-	-
	A_{Fe}	>8.0	-	-	-	-	-
	Refl _{frac}	11_{-4}^{+21}	-	-	-	-	-
	$\log(\rho/\text{cm}^{-3})$	<15.2	-	-	-	-	-
	norm ($\text{erg cm}^{-2} \text{s}^{-1}$)	$(3 \pm 2) \times 10^{-5}$	-	-	-	-	-
	C-stat/d.o.f.	279.5/275	256.8/267	174.0/158	200.2/227	47.0/33	12.2/7

Notes. Parameter values held fixed during the fit are given inside square brackets. We use a constant model to account for differences in normalization between each instrument and fix the constant for *NuSTAR*/PFMA spectra $C_{\text{FPMA}} = 1$ in each epoch. For the models `slimd` and `relxillCp`, the redshift of AT2018cow ($z = 0.01404$) is taken. We find that only for Epoch 4 adding a slim disk component significantly improves the fit compared to only using a power-law model (Table B.2). Nonetheless, we also test a model of a slim disk alone ("constant*TBabs*slimd") for Epoch 6, as the source becomes much softer at this epoch compared to previous epochs. The symbol "NC" means the parameter cannot be constrained within the allowed range of values (for θ this is $3^{\circ} \leq \theta \leq 90^{\circ}$, and for a_{\bullet} this is $-0.998 \leq a_{\bullet} \leq 0.998$). See Dauser et al. 2014 and García et al. 2014 for detailed descriptions of `relxillCp` parameters.

Table B.4: Same as Table B.3, but here we jointly fit all data from Epoch 2 to 6.

Model	Parameter	Epoch 1	Epoch 2	Epoch 3	Epoch 4	Epoch 5	Epoch 6
Constant	C_{FPMB}	0.96 ± 0.02	1.01 ± 0.03	0.92 ± 0.04	1.00 ± 0.06	-	-
	C_{Swift}	1.00 ± 0.05	0.95 ± 0.07	0.46 ± 0.08	0.9 ± 0.1	-	-
	$C_{\text{XMM-Newton}}$	-	-	-	0.79 ± 0.04	-	-
TBabs	$N_{\text{H}} (10^{20} \text{ cm}^{-2})$	[5.0]					
powerlaw	Γ	-	1.38 ± 0.02	1.52 ± 0.05	1.51 ± 0.05	$0.9^{+0.6}_{-1.1}$	-
	norm ($\text{keV}^{-1} \text{ cm}^{-2} \text{ s}^{-1}$)	-	$(10.0 \pm 0.5) \times 10^{-4}$	$(4.2 \pm 0.4) \times 10^{-4}$	$(2.7 \pm 0.3) \times 10^{-4}$	$(2.1 \pm 1.5) \times 10^{-6}$	-
slimdz	$\dot{m} (\dot{m}_{\text{Edd}})$	-	<4.9	<18	>4.8	<0.23	<0.17
	$\theta (^{\circ})$	-	-	-	<76	-	-
	$\log(M_{\bullet}/M_{\odot})$	-	-	-	$2.4^{+0.6}_{-0.1}$	-	-
	a_{\bullet}	-	-	-	$0.4^{+0.5}_{-0.9}$	-	-
relxillCp	$\theta (^{\circ})$	74 ± 2	-	-	-	-	-
	a_{\bullet}	0.98 ± 0.01	-	-	-	-	-
	kT_e (keV)	28 ± 8	-	-	-	-	-
	Γ	1.22 ± 0.02	-	-	-	-	-
	q	4 ± 2	-	-	-	-	-
	$\log(\xi)$	3.45 ± 0.06	-	-	-	-	-
	A_{Fe}	>8.0	-	-	-	-	-
	$\text{Refl}_{\text{frac}}$	11^{+21}_{-4}	-	-	-	-	-
	$\log(\rho/\text{cm}^{-3})$	<15.2	-	-	-	-	-
	norm ($\text{erg cm}^{-2} \text{ s}^{-1}$)	$(3 \pm 2) \times 10^{-5}$	-	-	-	-	-
	C-stat/d.o.f.	279.5/275		688.5/691			

Notes. We force the slim disk component in each epoch to have the same inclination θ , BH mass M_{\bullet} , and BH spin a_{\bullet} . Since statistically the slim disk component is not needed for Epoch 2, 3, and 5, only an upper limit on the disk accretion rate was obtained for those epochs.

Table B.5: Same as Table B.3, but here we jointly fit all data from Epoch 2 to 6, and we replace slimdz with slimbh.

Model	Parameter	Epoch 1	Epoch 2	Epoch 3	Epoch 4	Epoch 5	Epoch 6
Constant	C_{FPMB}	0.96 ± 0.02	1.01 ± 0.03	0.92 ± 0.05	1.00 ± 0.06	-	-
	C_{Swift}	1.00 ± 0.05	0.94 ± 0.07	0.47 ± 0.09	0.9 ± 0.1	-	-
	$C_{\text{XMM-Newton}}$	-	-	-	0.79 ± 0.04	-	-
TBabs	$N_{\text{H}} (10^{20} \text{ cm}^{-2})$	[5.0]					
powerlaw	Γ	-	1.38 ± 0.02	1.52 ± 0.05	1.57 ± 0.04	1.1 ± 0.3	-
	norm ($\text{keV}^{-1} \text{ cm}^{-2} \text{ s}^{-1}$)	-	$(10.0 \pm 0.5) \times 10^{-4}$	$(4.2 \pm 0.4) \times 10^{-4}$	$(3.1 \pm 0.2) \times 10^{-4}$	$(2.5^{+0.4}_{-0.7}) \times 10^{-6}$	-
slimbh	$L_{\text{disk}} (L_{\text{Edd}})$	-	<1.2	NC	>1.0	<0.07	<0.06
	$\theta (^{\circ})$	-	-	-	75 ± 8	-	-
	$\log(M_{\bullet}/M_{\odot})$	-	-	-	3.2 ± 0.2	-	-
	a_{\bullet}	-	-	-	<0.5	-	-
relxillCp	$\theta (^{\circ})$	74 ± 2	-	-	-	-	-
	a_{\bullet}	0.98 ± 0.01	-	-	-	-	-
	kT_e (keV)	28 ± 8	-	-	-	-	-
	Γ	1.22 ± 0.02	-	-	-	-	-
	q	4 ± 2	-	-	-	-	-
	$\log(\xi)$	3.45 ± 0.06	-	-	-	-	-
	A_{Fe}	>8.0	-	-	-	-	-
	$\text{Refl}_{\text{frac}}$	11^{+21}_{-4}	-	-	-	-	-
	$\log(\rho/\text{cm}^{-3})$	<15.2	-	-	-	-	-
	norm ($\text{erg cm}^{-2} \text{ s}^{-1}$)	$(3 \pm 2) \times 10^{-5}$	-	-	-	-	-
	C-stat/d.o.f.	279.5/275		691.8/691			

Notes. We force the slim disk component in each epoch to have the same inclination θ , BH mass M_{\bullet} , and BH spin a_{\bullet} . Furthermore, we replace slimdz with a pre-existing slim disk model slimbh. The total fit function for the joint-fit is then "constant*Tbabs*(powerlaw+slimbh)". See the main text for the physical differences between the models. Note in slimbh, $0.05 < L_{\text{disk}}/L_{\text{Edd}} < 1.25$ with $L_{\text{Edd}} \equiv 1.26 \times 10^{38} (M/M_{\odot}) \text{ erg/s}$, and only the prograde spin is considered ($a_{\bullet} > 0$). Both limb-darkening and surface profile are switched-on in slimbh during the fit (model switch vflag= 1 and lflag= 1), and the disk viscosity parameter $\alpha = 0.1$.

Table B.6: Joint-fits of *XMM-Newton*/EPIC-pn spectra from Epoch 5 and 6.

Model	Parameter	Epoch 5	Epoch 6	Model	Parameter	Epoch 5	Epoch 6
TBabs	N_{H} (10^{20} cm $^{-2}$)	[5.0]		TBabs	N_{H} (10^{20} cm $^{-2}$)	[5.0]	
powerlaw	Γ	$0.9^{+0.8}_{-3.1}$	-	powerlaw	Γ	$0.7^{+0.8}_{-3.2}$	-
	norm (keV $^{-1}$ cm $^{-2}$ s $^{-1}$)	$(190^{+171}_{-188}) \times 10^{-8}$	-		norm (keV $^{-1}$ cm $^{-2}$ s $^{-1}$)	$(151^{+181}_{-149}) \times 10^{-8}$	-
slimdz	\dot{m} (\dot{m}_{Edd})	<4.6	<3.6	slimbh	L_{disk} (L_{Edd})	<0.60	<0.17
	θ ($^{\circ}$)	NC $\{3^{\circ} \leq \theta \leq 90^{\circ}\}$			θ ($^{\circ}$)	NC $\{0^{\circ} \leq \theta \leq 85^{\circ}\}$	
	$\log(M_{\bullet}/M_{\odot})$	$2.5^{+1.4}_{-0.9}$			$\log(M_{\bullet}/M_{\odot})$	$2.2^{+1.0}_{-0.2}$	
	a_{\bullet}	NC $\{-0.998 \leq a_{\bullet} \leq 0.998\}$			a_{\bullet}	NC $\{0 < a_{\bullet} < 0.999\}$	
	C-stat/d.o.f.	57.7/39			C-stat/d.o.f.	57.3/39	

Notes. At these two epochs, the disk is likely to be at sub-Eddington mass accretion rates. We compare the results using the **slimdz** model with those using the **slimbh** model, employing a fit function of "**constant*TBabs*(powerlaw+slimdz)**" and a fit function of "**constant*TBabs*(powerlaw+slimbh)**", respectively. The symbol "NC" means the parameter cannot be constrained within the range of values allowed by models (listed in curly brackets).